

As-Grown Miniaturized True Zero-Order Waveplates Based on Low-Dimensional Ferrocene Crystals

Zhipeng Li, Xuezhi Ma,* Fengxia Wei, Dapeng Wang, Zeyu Deng, Mengting Jiang, Arif Siddiquee, Kun Qi, Di Zhu, Meng Zhao, Mengzhe Shen, Pieremanuele Canepa, Shanshan Kou,* Jiao Lin,* and Qian Wang*

As basic optical elements, waveplates with anisotropic electromagnetic responses are imperative for manipulating light polarization. Conventional waveplates are manufactured from bulk crystals (e.g., quartz and calcite) through a series of precision cutting and grinding steps, which typically result in large size, low yield, and high cost. In this study, a bottom-up method is used to grow ferrocene crystals with large anisotropy to demonstrate self-assembled ultrathin true zero-order waveplates without additional machining processing, which is particularly suited for nanophotonic integration. The van der Waals ferrocene crystals exhibit high birefringence (Δn (experiment) = 0.149 ± 0.002 at 636 nm), low dichroism $\Delta\kappa$ (experiment) = -0.0007 at 636 nm), and a potentially broad operating range (550 nm to 20 μm) as suggested by Density Functional Theory (DFT) calculations. In addition, the grown waveplate's highest and the lowest principal axes (n_1 and n_3 , respectively) are in the a - c plane, where the fast axis is along one natural edge of the ferrocene crystal, rendering them readily usable. The as-grown, wavelength-scale-thick waveplate allows the development of further miniaturized systems via tandem integration.

realized significant advancements, such as in metalenses,^[2] flat differentiators,^[3] integrated photodetectors,^[4] meta-filters,^[5] and ultra-compact spectrometers.^[6] However, waveplates in the wavelength scale remain underdeveloped as one of the most essential optical components for manipulating light polarization. An urgent demand exists for compact optical systems to be used in dynamic polarization control,^[7] optical interconnect chips,^[8] on-chip quantum information processing,^[9] all-optical neuromorphic computing,^[10] and lab-on-chip light sources.^[11]

Polarization control relies on the birefringence yielded by the inherent anisotropic properties of the material. An ideal miniaturized waveplate requires an ultrathin thickness (high birefringence, Δn), low loss (small extinction coefficients, κ), low distortion (low dichroism, $\Delta\kappa$), and ease of fabrication. In addition, unlike conventional multi-order waveplates, true zero-order waveplates, which provide

retardance within 2π , are naturally thin and offer additional advantages such as large-angle acceptance and high tolerances for changing the temperature and humidity.^[12] Thus, the fabrication of miniaturized true zero-order waveplates necessitates the identification of the appropriate materials with large Δn , small κ ,

1. Introduction

The miniaturization of bulk optical components can render optical systems more compact, efficient, and energy efficient.^[1] In this regard, the optics and photonics communities have

Z. Li, X. Ma, F. Wei, M. Jiang, D. Zhu, M. Zhao, Q. Wang
Institute of Materials Research and Engineering (IMRE)
Agency for Science, Technology and Research (A*STAR)
2 Fusionopolis Way, Innovis, #08-03, Singapore 138634, Singapore
E-mail: ma_xuezhi@imre.a-star.edu.sg; wangqian@imre.a-star.edu.sg


D. Wang, M. Shen
Institute of Biointelligence Technology
BGI-Research Shenzhen
Shenzhen 518083, China

Z. Deng, P. Canepa
Department of Materials Science and Engineering
National University of Singapore
Singapore 117575, Singapore

A. Siddiquee, S. Kou
Department of Chemistry and Physics
La Trobe Institute for Molecular Science (LIMS)
La Trobe University
Victoria 3086, Australia
E-mail: s.kou@latrobe.edu.au

K. Qi
Institut Européen des Membranes
IEM
UMR 5635
Université Montpellier
ENSCM
CNRS
Montpellier 34000, France

J. Lin
School of Engineering
RMIT University
Victoria 3000, Australia
E-mail: jiao.lin@rmit.edu.au

 The ORCID identification number(s) for the author(s) of this article can be found under <https://doi.org/10.1002/adma.202302468>

DOI: 10.1002/adma.202302468

and low $\Delta\kappa$. Naturally occurring birefringent crystals with high birefringence, such as calcite (CaCO_3 , $\Delta n \sim 0.17$ at 630 nm)^[13] and rutile (TiO_2 , $\Delta n \sim 0.28$ at 632.8 nm)^[14] However, their intricate crystal structures and high mechanical hardness render it difficult to form a flat layer of true zero-order waveplates via uniform deposition or mechanical grinding.^[15] Some artificial birefringent crystals, such as yttrium orthovanadate (YVO_4),^[16] lithium niobate (LiNbO_3),^[17] and α -BBO ($\alpha\text{-BaB}_2\text{O}_4$)^[18] are affected by similar fabrication difficulties. Additionally, in-plane anisotropic materials such as black phosphorus (BP)^[7] rhenium disulfide (ReS_2),^[19] rhenium diselenide (ReSe_2),^[20] and titanium trisulfide (TiS_3),^[21] are unqualified for the ideal waveplate because of either the overall energy dissipation or inconsistent absorption coefficients in the visible and near-infrared range. Moreover, the anisotropy of most 2D materials is caused by significant differences between their interlayer covalent and intralayer van der Waals bonds.^[22] Thus, obtaining a large in-plane (a–c plane) birefringence in these materials is difficult, which hinders their broad application. To date, birefringent quartz is the only commercially available true zero-order waveplate.^[13] Owing to its low birefringence ($\Delta n \sim 0.008$ at 636 nm), the waveplate thickness is limited to $\approx 25 \mu\text{m}$, which is extremely large for the miniaturization of optical components. In addition to inorganic birefringent materials, organic materials like liquid crystal polymer (LCP) have proven their worth as zero-order waveplates, thanks to their significant birefringence and low dichroism.^[23] Additionally, the LCP film can be processed simply through spin-coating and polarized UV light-curing activation, making it compatible with flexible and stretchable applications.^[24] However, miniaturization and chip integration are challenging to achieve with the spin-coating process for LCP waveplates, limiting their potential in integrated photonics systems. Alternatively, metasurfaces can directly manipulate the phase of light and be designed to achieve a broad operating wavelength range.^[25] Furthermore, MEMS-based metasurfaces are capable of achieving tunable waveplates for dynamic tasks, making them promising for next-generation photonic chips.^[26] However, metasurfaces necessitate specialized designs, complex nanofabrication processes with subwavelength resolution, and relatively low conversion efficiencies, which hinder their widespread application.^[27] Therefore, identifying easily processable materials with relatively high birefringence, low extinction coefficients, and low dichroism to construct on-chip waveplates is critical for ensuring highly efficient integrated photonics systems.

In this context, ferrocene ($\text{Fe}(\text{C}_5\text{H}_5)_2$), which is well-acknowledged as a sandwich compound that is first revealed by Ernst Otto Fischer and Geoffrey Wilkinson,^[28] exhibits interesting optical properties owing to its unique structure. Hence, we demonstrate an as-grown ferrocene crystal that accomplishes a true zero-order waveplate with wavelength-scale thickness. The grown orientation of ferrocene crystal can be adjusted along the principle refractive axis, thus enabling the ideal waveplate architecture without additional processing. **Figure 1a** shows the concepts of the as-grown quarter-and-half waveplates with ultraslim thicknesses of 1071 and 2142 nm, which can convert light among circular, elliptical, and linear polaritons. The fast axis of the as-grown waveplate is along one natural edge of the ferrocene single crystal (the optical microscope image of the crystal is shown in the top right corner). The ultrathin nature

of layered waveplates enables the development of miniaturized systems via tandem integration.

2. Results and Discussion

2.1. Ferrocene Crystal Structure

Ferrocene molecules can self-assemble to form a monoclinic crystal structure, which is a typical biaxial crystal structure with high birefringence^[29] (for growth methods, see Section S1, Supporting Information); thus, they can be used to form efficient waveplates for miniaturized devices. To investigate the origin of the large anisotropy, the molecular structures along the a-, b-, and c-axes were examined, as shown in Figure 1b–d, respectively, which indicated a 3D van der Waals force-bounded material.

We used density function theory (DFT)-calculated refractive indices along the $\langle 100 \rangle$, $\langle 010 \rangle$, $\langle 001 \rangle$, $\langle 110 \rangle$, $\langle 101 \rangle$, $\langle 011 \rangle$, and $\langle 111 \rangle$ directions to reconstruct the refractive-index ellipsoid (Figure 1e). The b-axis was perpendicular to the a–c plane, and the angle between the a- and c-axes was 120.95° . In particular, the highest and lowest principal axes (n_1 and n_3 , respectively) were in the a–c plane (the reconstruction method is described in the Experimental Section). Hence, the largest anisotropy, and the most efficient phase retarder, appeared in the a–c plane, as verified via single-crystal X-ray diffraction (SC-XRD) (See Section S2, Supporting Information). Consequently, bar-like ferrocene crystals grown along the b-axis can be used directly as waveplates. In addition to its monoclinic crystal structure, the high birefringence of ferrocene originated from the strong anisotropic polarizability induced by the delocalized π -conjugated orbitals of Fe^+ ions. In the ferrocene molecule (Figure 1f), the two five-membered rings were connected by a Fe^+ ion, and the two rings exhibited a twisted angle of 36° , which induced strong structural anisotropy. The large anisotropy was reflected in the electronic wave functions of ferrocene in the highest occupied molecular orbitals (HOMO) and lowest unoccupied molecular orbitals (LUMO) (Figure 1g).

Figure 2a shows the calculated projected density of states (PDOS) of C-2p, H-1s, and Fe-3d denoted in red, yellow, and blue, respectively. The electrons in ferrocene showed some allowed transitions from the valence bands to conduction bands, including from the HOMO (also recognized as a'_{1g} orbitals) to the LUMO (also recognized as e'_{1g} orbitals), from e_{2g} orbitals to e'_{1g} orbitals, and other higher-order transitions (for more details, see Section S3, Supporting Information). These transitions resulted in significant absorption near the corresponding photon energies. We used DFT to calculate the wavelength-dependent real and imaginary components of the refractive index along the principal axes of the ferrocene single crystals, as shown in Figures 2b and c, respectively. Although ferrocenes exhibit high birefringence near the bandgap region, such as $\Delta n = 0.27$ at 441 nm corresponding to the first allowed transition of electrons, the high absorption losses and large distortion ($\kappa_1 = 0.049$, $\Delta\kappa = 0.025$) limit their optical applications near the wavelength range.

To determine the optimal operating wavelength range for the ferrocene waveplates, we used the Kramers–Kronig (K–K) relation to guide the application strategy and avoid large absorption and dichroism regions. The K–K relation describes the bidirectional mathematical relations connecting the real and imaginary

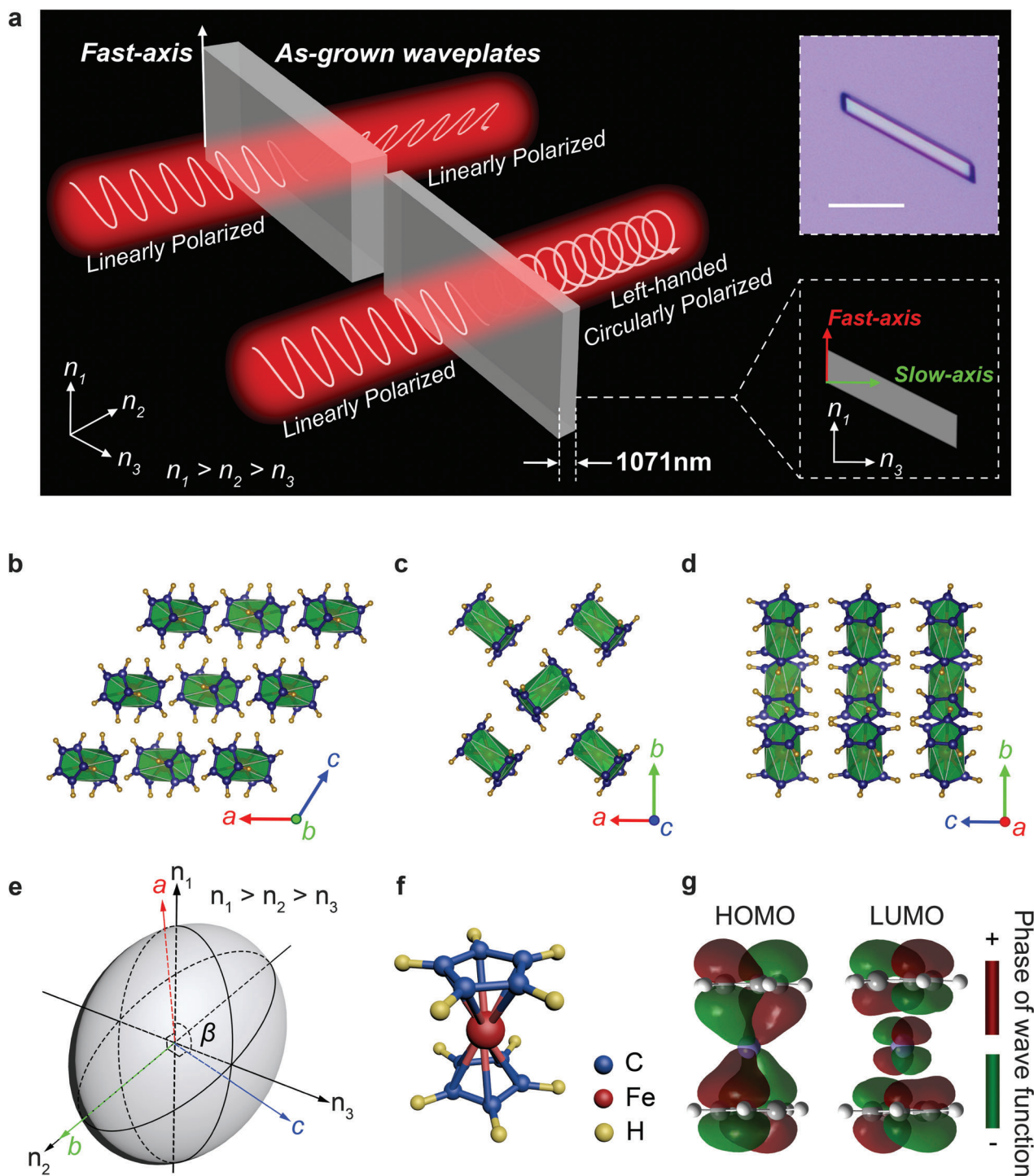


Figure 1. As-grown miniaturized true zero-order waveplates based on 3D van der Waals ferrocene crystals. a) Concept of as-grown true zero-order ferrocene quarter and half waveplates with a thickness of 1071 and 2142 nm, respectively. Light can be converted among circular, elliptical, and linear polarizations using ferrocene waveplates with different thicknesses. Fast axis of waveplate is oriented along one natural edge of the ferrocene crystal. Top right corner shows an optical microscope image of the ferrocene crystal; lower right corner shows a schematic illustration of the fast- and slow axes of the waveplate. The scale bar is 20 μm . b–d) Ferrocene crystal structure viewed along b) b-axis, c) c-axis, and d) a-axis. Blue, yellow, and brown spheres represent carbon, hydrogen, and iron atoms, respectively. Ferrocenes crystals exhibit P21/a symmetry, with $a = 10.443 \text{ \AA}$, $b = 7.572 \text{ \AA}$, $c = 5.824 \text{ \AA}$ and $\beta = 120.95^\circ$. e) Refractive index ellipsoid reconstructed from density functional theory (DFT) calculations, where the b-axis of the ferrocene crystal is parallel to one of the principal refractive indices. f) Molecular structure of ferrocene shows a sandwich structure, where carbon atoms are placed at the corners of two plates surrounding an iron atom, and the two plates exhibit a 36° twisted angle. g) HOMO (the highest-occupied molecular orbitals) and LUMO (the lowest-unoccupied molecular orbitals) of ferrocene exhibit a significant difference in symmetry, which implies the high polarizability of the molecular structure and hence high birefringence.

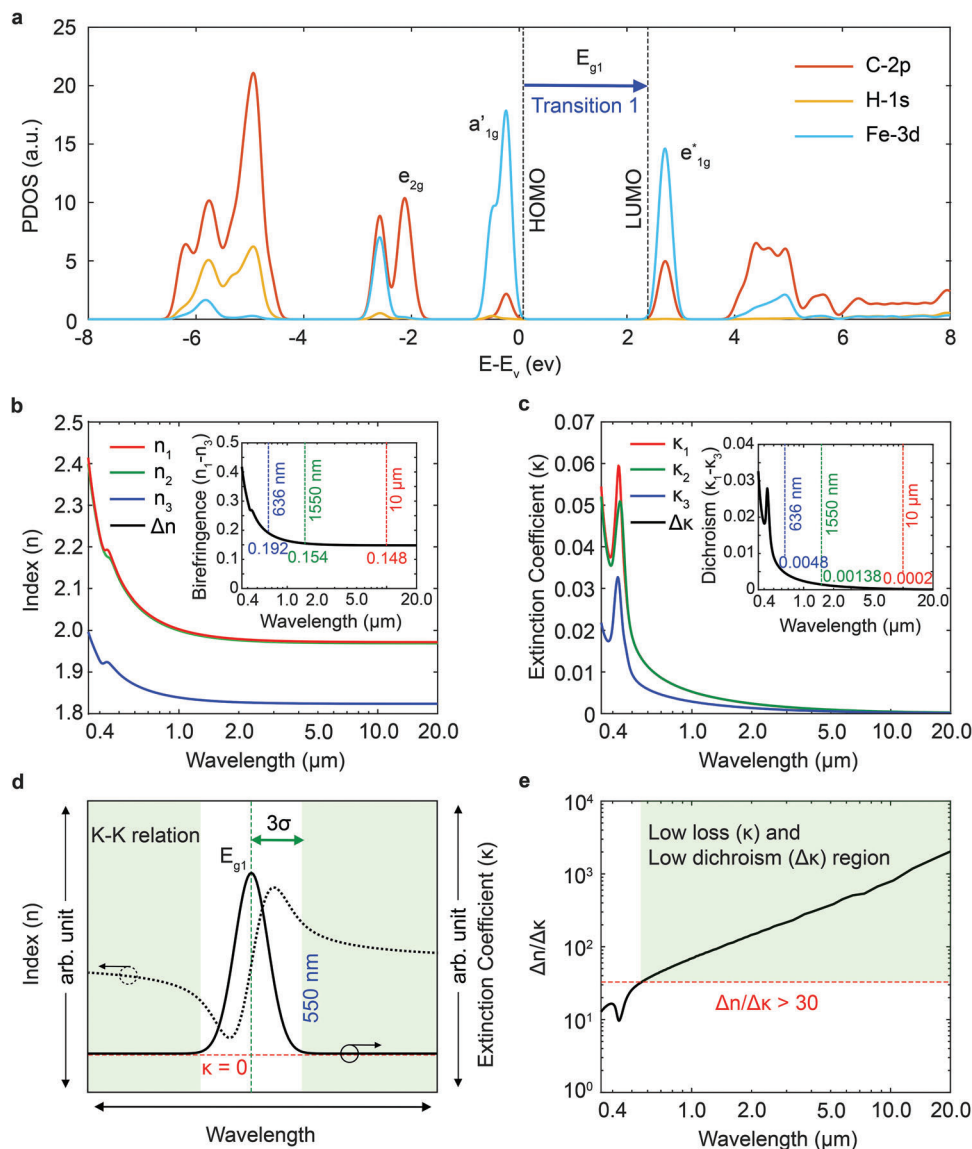


Figure 2. DFT calculations and Kramers–Kronig relations. a) Projected density of states of ferrocene. E_{g1} is the bandgap corresponding to the energy of electron transition from HOMO to LUMO. b,c) DFT-calculated refractive index (n) and extinction coefficient (κ) along principal axes of ferrocene single crystal. The birefringence ($n_1 - n_3$) and dichroism ($\kappa_1 - \kappa_3$), shown in the upper right inset, exhibit a high birefringence of 0.192 and a low dichroism of 0.0048 at 636 nm. d) Gaussian-shaped κ peak corresponding to bandgap E_{g1} , and n_1 calculated from Kramers–Kronig (K–K) relations. Green highlighted area represents the operating wavelength range of the ferrocene waveplate, based on the proposed criterion of 3σ beyond the Gaussian peaks of κ to identify low- κ and high- n regions. e) $\Delta n/\Delta\kappa$ calculated from (b) and (c) shows the excellent optical performance of ferrocene waveplates in a broad wavelength region from 550 nm to 20 μm ($\Delta n/\Delta\kappa > 30$).

components of any complex function that satisfies causality.^[30] The κ (imaginary component of the refractive index) of ferrocene can be decomposed into a sequence of Gaussian peaks corresponding to different allowed orbital transitions. The full wavelength range of κ is provided in Figure S4 (Supporting Information). The Gaussian peak corresponding to E_{g1} is shown in Figure 2d ($\kappa(E_{g1})$, solid black curve), where the transformed $n(E_{g1})$ using the K–K relation shows an asymmetric peak. We propose to select the region from $\pm 3\sigma$ of the Gaussian peaks in κ (the green region in Figure 2d), where ferrocene exhibits negligible κ and $\Delta\kappa$ but maintains large Δn and $\Delta n/\Delta\kappa (> 30$ in this region, Figure 2e).

2.2. Optical Demonstration of Waveplates Based on Ferrocene Single Crystals

The retardance of ferrocene single crystals ($\delta = \frac{2\pi}{\lambda} \Delta n \times t$) is thickness dependent, where λ is the vacuum wavelength of light, and t denotes the thickness of the crystals along the b-axis. Alternately, retardance can be represented as $\delta = \pm (m \times 2\pi + \phi)$, where $m = 0, 1, 2, 3, \dots$ and $0 \leq \phi \leq 2\pi$, and the ϕ can be recognized as net retardance. The waveplates are of true zero order when $m = 0$, whereas the thickness is minimized compared with their higher-order counterparts with the same net retardance, thus rendering them suitable for on-chip

integration. The retardancy and birefringence were characterized using the two-frame method^[31] and the corresponding optical characterization protocol (see Experimental Section and Supplementary Section S5, Supporting Information). Atomic force microscopy (AFM, Neaspec GmbH) and a surface profiler were used to characterize ferrocene crystal in two thickness ranges, i.e., 0–2.5 μm and greater than 2.5 μm. The light source used in this measurement had a center wavelength of 636 nm and a bandwidth of 20 nm (Thorlabs, M625L4). **Figure 3a** shows the measured results for the retardance of ferrocene crystals with various thicknesses. The obtained birefringence of ferrocene was 0.149 ± 0.002 at 636 nm, which was slightly smaller than the value calculated via DFT. The DFT typically underestimates the bandgap; therefore, the calculated refractive index curves are redshifted compared with the experimental results, thus resulting in slightly higher calculated values of Δn , κ , and $\Delta\kappa$.^[32] We selected three representatives from the aforementioned waveplates shown in **Figure 3a**, namely, the quarter waveplate, 1/3 waveplate, and half waveplate, and extracted their retardance. The waveplates can convert incident right-hand circularly polarized (RCP) light to linearly polarized, elliptically polarized, and left-hand circularly polarized (LCP) light, as indicated by the trajectories on the Poincaré sphere (**Figure 3b**). The transmission images of the waveplates presented in (i) and (ii) show high, medium, and low contrasts after the quarter, 1/3, and half waveplates, respectively, which reflect the high performance of the waveplates. The calculated phase retardance is shown in **Figure 3c–e**(iii) (for the phase calculation, see Section S5, Supporting Information). The two ferrocene single crystals at the same optical window in **Figure 3c**(iii) show retardances of $\pi/2$ and $-\pi/2$, respectively. As verified via SC-XRD and AFM, their fast axes (n_1) were parallel to each other, whereas their slow axes (n_3) have opposite sign, indicating that they served as quarter and 3/4 waveplates, respectively.

Low κ and $\Delta\kappa$ values are equally important for a waveplate. These values were extracted from the measured absorption spectra. We used a UV–vis–NIR microspectrophotometer (CRAIC Technologies) to measure the transmission (T) and reflection (R) spectra of selected small regions and calculated the absorption (A) of the ferrocene plates. The normalized absorbance is expressed as $A(\text{norm}) = \frac{1-T-R-L}{t}$, where t denotes the thickness of the ferrocene single crystals and L is the thickness-independent loss from the multi-interface reflection of the sample and substrate, which was extracted from 15 ferrocene crystal absorbance measurements. Meanwhile, κ can be calculated from the formula $\kappa = \frac{\ln(10) \times A \times \lambda}{4\pi \times t}$ (Raw data and more calculation details are available in Section S8, Supporting Information). **Figure 3f** shows ultra-low losses $\kappa_1 = 0.0031$ and $\kappa_3 = 0.0038$ at 636 nm along the fast- and slow-axes of the ferrocene waveplate, respectively. The normalized $\Delta\kappa$ is approximately zero (e.g., -0.0007 at 636 nm) in the waveplate operating wavelength range (green region, defined in **Figure 2**) shown in **Figure 3g**, thus indicating that ferrocene single crystals can serve as top-tier waveplates.

2.3. Determination of Fast- and Slow-Axes of Waveplates

To demonstrate the quarter-waveplate functionalities, we performed optical measurements of the ferrocene crystals using a modified two-frame phase characterization setup. First, we iden-

tified the fast axis of the ferrocene waveplate and then preserved 45° between the linearly polarized input light and the quarter-waveplate fastaxis (Further details of the measurement protocols are available in Section S9, Supporting Information). Based on these processes, the ferrocene quarter-waveplate converts the linearly polarized input light into circularly polarized output light, whereas the background (transmitted through the x-cut quartz substrate) maintains a linearly polarized state. We recorded the transmission images by rotating the analyzer's linear polarizer in intervals of 10°; six representative images are shown in **Figure 4a**. The quarter waveplate we measured (as shown in **Figure 4**) introduced a retardance of 84.1° with a thickness of 1000 ± 0.5 nm. The average intensities from the sample and substrate were extracted and fitted using the ellipse equation ($r = \frac{ab}{\sqrt{a^2 \cos^2 \theta + b^2 \sin^2 \theta}}$) and cosine equation ($r = c \cdot \cos [2(\theta - d)]$) to identify the fast- and slow-axes of the ferrocene waveplate (**Figure 4b**). Based on the fitting, the input linearly polarized light (φ_0) and the fast axis (θ_0) of the waveplate form a $44.5^\circ \pm 0.1^\circ$ angle instead of 45° for the ideal case, which is within the experimental error range. Results show that the fast axes of the waveplates were highly aligned with the direction of the naturally grown short sides of the self-assembled ferrocene single crystals. As illustrated in **Figure 4c**, the c-axis was strictly aligned with the long side of the ferrocene crystal, as indicated by SC-XRD (see Section S2, Supporting Information), and the angle between the two naturally grown sides was $65.0^\circ \pm 2.0^\circ$ (see Section S10, Supporting Information). As the angle between the a- and c-axes was 59.05°, the angle between the fast-axis (n_1) and a-axis θ (experiment) was $5.95^\circ \pm 2.0^\circ$, which agreed well with the value calculated via DFT (6.91°). In summary, self-assembled ferrocene crystals can serve as true zero-order waveplates with naturally grown fast axes, thus facilitating their direct use.

3. Conclusion

The miniaturization of waveplates can downsize the increasingly complex optical systems required for advanced photonic information processing and computing applications. We used a bottom-up method to grow ferrocene crystals, which self-assembled at the liquid–liquid capillary interface. The special molecular arrangement in the structure enabled a high birefringence (Δn (DFT) = 0.192, Δn (experiment) = 0.149 ± 0.002), low dichroism ($\Delta\kappa$ (DFT) = 0.0048, $\Delta\kappa$ (experiment) = -0.0007) at 636 nm and a potentially broad operating range (550 nm to 20 μm). In particular, the self-assembled ferrocene crystals exhibit facet orientations along the b-axis at the acetone–water capillary interface. The naturally grown a–c planes exhibit the highest birefringence ($n_1 - n_3$) and can be directly used as on-chip true zero-order waveplates. Using the thickness control method during the self-assembly process allows various retardants of the ferrocene waveplate to be designed and controlled.

These prominent optical properties may be extendable to other members of the metallocene family, such as nickelocenes, cobaltocenes, and ruthenocenes, which exhibit similar sandwich molecular structures. Moreover, metallocene derivatives such as multi-decker sandwich compounds^[33] and metallocenes^[34] are expected to demonstrate significant potential in this field. By deploying the K–K relations, candidates possessing high

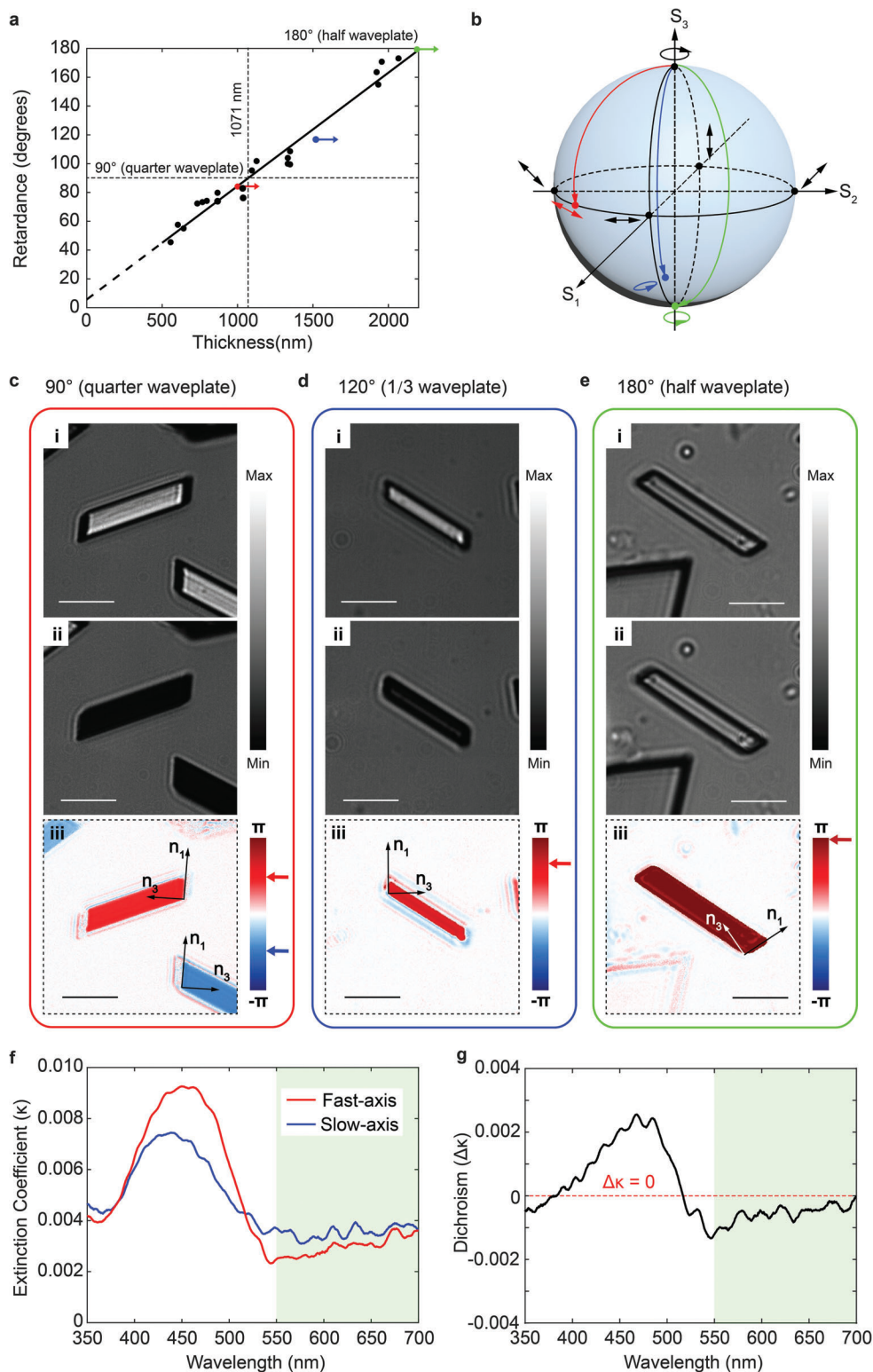


Figure 3. Optical demonstration of true zero-order waveplates based on ferrocene crystal. a) Measured retardance of ferrocene waveplates as a function of thickness of crystals along b-axis. Birefringence of ferrocene crystal at 636 nm was calculated to be 0.149 ± 0.002 via linear fitting of 23 samples. An ideal quarter waveplate (90° of retardance) was achieved when the crystal thickness was 1071 nm. b) Poincaré sphere shows polarization change trajectories for three representative waveplates, as indicated in the a: quarter, 1/3, and half waveplates. c–e) Optical property characterization of three ferrocene crystal waveplates using the two-frame method. Circularly polarized incident light can be converted into linearly, elliptically, and linearly polarized light, separately. (i) and (ii) show optical images of waveplates in on and off states, and (iii) shows the retracted retardance map. f,g) κ and $\Delta\kappa$ values of ferrocene crystals measured using UV–visible–NIR microspectrophotometer (window size $1.6 \mu\text{m} \times 1.6 \mu\text{m}$). All scale bars are $30 \mu\text{m}$.

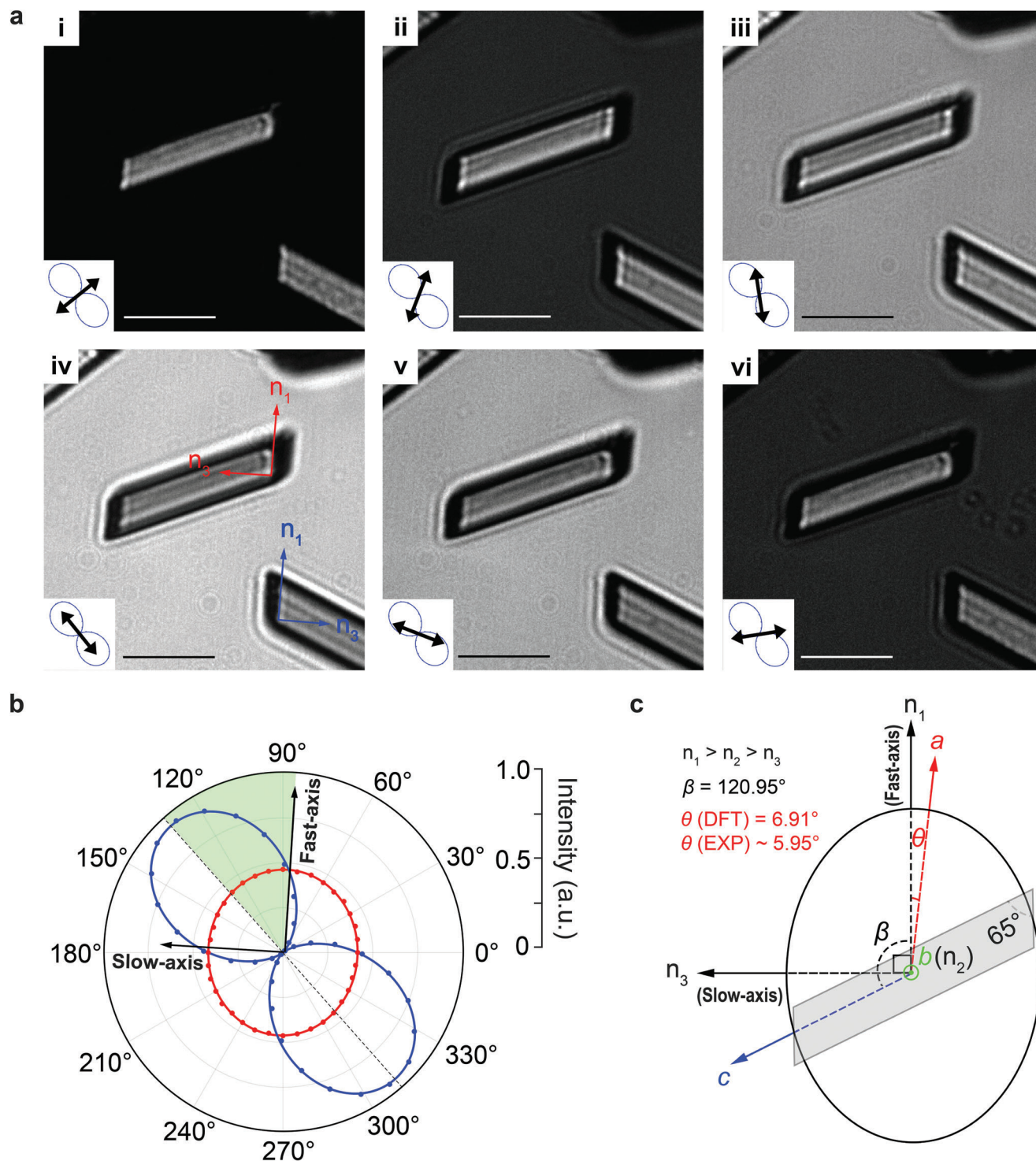


Figure 4. Determination of fast- and slow-axes of waveplates. a) Images of ferrocene waveplate after analysis of linear polarizer with various angles (directions are shown in lower left corner of each panel). Similar intensities of waveplate image indicate the quarter waveplate function for converting linearly polarized light to circularly polarized light. b) Angle-resolved transmission intensity of ferrocene quarter waveplate and substrate, where the intensities of the transmitted light from the ferrocene waveplate present an almost circular shape instead of a cosine-like profile from the background. The angle between the fast axis of the ferrocene waveplate and the direction of the linearly polarized incident light is 45° . c) Retracted fast- and slow-axis directions. Fast axis is coincidentally parallel to short side of ferrocene crystals. All scale bars are $30\ \mu\text{m}$.

birefringence and low dichroism in a suitable wavelength range can be identified, thereby accelerating the material screening process. The material exploration strategy presented herein allows nanoscale polarization to be manipulated and is promising for the mass production of low-dimensional multifunctional optical devices.

4. Experimental Section

Preparation of Ferrocene Crystals: Ferrocene crystals were prepared using the liquid–liquid interfacial precipitation method (more details are presented in Section S1, Supporting Information). Ferrocene powder (Sigma–Aldrich, 98% purity, CAS: 102-54-5) was dissolved in acetone (ACS reagent, 99.5% purity), and the ferrocene solution was deposited into deionized water to form ferrocene crystal nuclei. To remove the irregular nucleus, the mixture was heated up (80 °C for the first cycle and 50 °C for the remaining four cycles) and cooled down (0 °C) for five cycles (Section S1.2, Supporting Information). Subsequently, one drop of the resulting mixture was deposited onto the targeting substrate, and the nucleus seed was grown on the substrate upon acetone evaporation. Finally, ferrocene crystals were obtained on the substrate by removing the liquid using a spinner.

Optical Measurement: The optical characterization setup comprises two operating modes: the two-frame mode^[31] for extracting the birefringence and the angle-resolved polarization analysis mode. Figure S5 (Supporting Information) shows the two-frame mode, in which the angle-resolved polarization analysis mode can be obtained by removing the quarter-wave plate. In the setup, a collimated LED (M625L4, Thorlabs) was used as the light source with a central wavelength of 636 nm and a linewidth of 20 nm. A Glan-Laser Polarizer (GL10, Thorlabs) was placed in front of the LED to ensure that the light was perfectly linearly polarized. A Fresnel rhomb retarder (FR600HM, Thorlabs) was used as a half-wave plate to rotate the linearly polarized light in an arbitrarily polarized direction. A quarter-waveplate (WPMQ05M-633, Thorlabs) equipped with a reversed beam expander (shrinker) was used to project circularly polarized light with a shrinking beam size onto the ferrocene samples. An objective lens (20 × Mitutoyo Plan Apo Infinity Corrected Long WD objective, NA = 0.42, corresponding tube lens, f = 200 mm) and 16-bit high-sensitivity camera (Zyla 5.5, Andor) were used for the imaging system. The linear polarizer was mounted on a high-precision rotation stage (PR01, Thorlabs) with 360° rotation capability to select the desired polarization state for ferrocene imaging.

DFT Calculation: Spin-polarized DFT calculations of the molecular structure were performed using the Vienna ab initio Simulation Package.^[35] Projector-augmented wave potentials were used, with the following electrons treated explicitly: H (1s¹), C (2s²2p²), and Fe (3d⁶4s²).^[36] The exchange and correlation components of the Kohn–Sham equation were calculated using the generalized gradient approximation,^[37] and the van der Waals forces were corrected using the Grimme scheme.^[38] A 520-eV kinetic energy cut-off and a 3 × 2 × 2 Monkhorst-Pack K-point mesh^[39] were used for all calculations. The crystal structure of ferrocene was first relaxed based on previous experimental results^[40] until the interatomic forces were smaller than 0.01 eV Å⁻¹. Subsequently, the PDOS and the frequency-dependent dielectric function were obtained after the electronic ground state was determined. The refractive indices (*n*) and extinction coefficients (*κ*) were determined as follows:

$$n = \frac{1}{\sqrt{2}} \left((\epsilon_r^2 + \epsilon_i^2)^{\frac{1}{2}} + \epsilon_r \right)^{\frac{1}{2}} \quad (1)$$

$$\kappa = \frac{1}{\sqrt{2}} \left((\epsilon_r^2 + \epsilon_i^2)^{\frac{1}{2}} - \epsilon_r \right)^{\frac{1}{2}} \quad (2)$$

where ϵ_r and ϵ_i are the real and imaginary components of the complex dielectric function (ϵ), respectively.

Statistical Analysis: For the reconstruction of the index ellipsoid, the following statistical method was used. Most of the materials with monoclinic structures, such as α -BIBO (α -BiB₃O₃),^[29a] TbCOB (TbCa₄O(BO₃)₃),^[29b] and Yb³⁺ doped magnesium tungsten oxide (Yb: MgWO₄),^[29c] are biaxial crystals with their b-axes parallel to the direction of one of the principal refractive indices in index ellipsoid (also known as optical indicatrix). Thus, the other two principal refractive indices will fall into the a–c plane. The DFT calculation was used and the refractive indices were extracted along <100>, <010>, <001>, <110>, <101>, <011>, and <111> directions, where <100>, <001>, and <101> directions were in the a–c plane. Using the ellipse equation, the long axis and short axis of the ellipse could be extracted, namely *n*₁ and *n*₃ in the current case. MATLAB 2022b was used to analyze the data.

Supporting Information

Supporting Information is available from the Wiley Online Library or from the author.

Acknowledgements

This research was supported by the Agency for Science, Technology, and Research (A*STAR) under its AME IRG Fund (Grant No. A20E5c0095), and Career Development Fund (Grant No. C210112044, C210112054, and C210812027), and Career Development Fund-Seed Projects (Grant No. 222D800038).

Conflict of Interest

The authors declare no conflict of interest.

Code Availability

All codes used in the main text and Supporting Information are available from the corresponding author upon request.

Author Contributions

Z.L., X.M., and F.W. contributed equally to this study. Z.L., X.M., J.L., and Q.W. conceived the study. Q.W., X.M., J.L., and S.K. supervised the study. Z.L. synthesized ferrocene crystals with the assistance of M.J. X.M. performed optical characterization with the assistance of Z.L., Z.D. performed DFT simulations. X.M. analyzed the data with the assistance of Z.L., F.W., and Z.D. Z.L. and F.W. performed SC-XRD, Raman, and XRD characterizations. X.M. and Q.W. wrote the manuscript with the assistance of F.W., Z.L., J.L., and D.Z. All authors have discussed the results and read the manuscript.

Data Availability Statement

All data that support the findings of this study are available in the main text, figures, and Supplementary Information. They are also available from the corresponding author upon reasonable request.

Keywords

anisotropy, birefringence, ferrocenes, self-assembly, true zero-order waveplates

Received: March 16, 2023

Revised: May 12, 2023

Published online: June 25, 2023

- [1] a) A. W. Elshaari, W. Pernice, K. Srinivasan, O. Benson, V. Zwiller, *Nat. Photonics* **2020**, *14*, 285; b) J. Kim, G. Sahay, *Nat. Nanotechnol.* **2022**, *17*, 1.
- [2] W. T. Chen, A. Y. Zhu, F. Capasso, *Nat. Rev. Mater.* **2020**, *5*, 604.
- [3] Y. Zhou, H. Zheng, I. I. Kravchenko, J. Valentine, *Nat. Photonics* **2020**, *14*, 316.
- [4] L. Li, H. Lin, Y. Huang, R.-J. Shiue, A. Yadav, J. Li, J. Michon, D. Englund, K. Richardson, T. Gu, J. Hu, *Optica* **2018**, *5*, 44.
- [5] M. N. Julian, C. Williams, S. Borg, S. Bartram, H. J. Kim, *Optica* **2020**, *7*, 746.
- [6] Z. Yang, T. Albro-Owen, H. Cui, J. Alexander-Webber, F. Gu, X. Wang, T. C. Wu, M. Zhuge, C. Williams, P. Wang, A. V. Zayats, W. Cai, L. Dai, S. Hofmann, M. Overend, L. Tong, Q. Yang, Z. Sun, T. Hasan, *Science* **2019**, *365*, 1017.
- [7] S. Biswas, M. Y. Grajower, K. Watanabe, T. Taniguchi, H. A. Atwater, *Science* **2021**, *374*, 448.
- [8] P. Chaisakul, D. Marris-Morini, J. Frigerio, D. Chrastina, M.-S. Rouifed, S. Cecchi, P. Crozat, G. Isella, L. Vivien, *Nat. Photonics* **2014**, *8*, 482.
- [9] G. Zhang, J. Y. Haw, H. Cai, F. Xu, S. M. Assad, J. F. Fitzsimons, X. Zhou, Y. Zhang, S. Yu, J. Wu, W. Ser, L. C. Kwek, A. Q. Liu, *Nat. Photonics* **2019**, *13*, 839.
- [10] V. K. Sangwan, M. C. Hersam, *Nat. Nanotechnol.* **2020**, *15*, 517.
- [11] X. Ma, K. Kudtarkar, Y. Chen, P. Cunha, Y. Ma, K. Watanabe, T. Taniguchi, X. Qian, M. C. Hipwell, Z. J. Wong, S. Lan, *Nat. Commun.* **2022**, *13*, 6916.
- [12] a) S. M. Wilson, V. Vats, P. H. Vaccaro, *J. Opt. Soc. Am. B* **2007**, *24*, 2500; b) J. Liu, Y. Cai, H. Chen, X. Zeng, D. Zou, S. Xu, *Opt. Express* **2011**, *19*, 8557; c) P. D. Hale, G. W. Day, *Appl. Opt.* **1988**, *27*, 5146.
- [13] R. N. Smartt, W. H. Steel, *J. Opt. Soc. Am.* **1959**, *49*, 710.
- [14] W. M. Sinton, *J. Opt. Soc. Am.* **1961**, *51*, 1309_1.
- [15] a) Y. Y. Kim, A. S. Schenk, J. Ihli, A. N. Kulak, N. B. J. Hetherington, C. C. Tang, W. W. Schmahl, E. Griesshaber, G. Hyett, F. C. Meldrum, *Nat. Commun.* **2014**, *5*, 4341; b) T. Kubo, H. Orita, H. Nozoye, *J. Am. Chem. Soc.* **2007**, *129*, 10474.
- [16] H. T. Luo, T. Tkaczyk, E. L. Dereniak, K. Oka, R. Sampson, *Opt. Lett.* **2006**, *31*, 616.
- [17] D. E. Zelmon, D. L. Small, D. Jundt, *J. Opt. Soc. Am. B* **1997**, *14*, 3319.
- [18] J. R. DeVore, *J. Opt. Soc. Am.* **1951**, *41*, 416.
- [19] D. Akinwande, C. Huyghebaert, C. H. Wang, M. I. Serna, S. Goossens, L. J. Li, H. P. Wong, F. H. L. Koppens, *Nature* **2019**, *573*, 507.
- [20] H. Yang, H. Jussila, A. Autere, H.-P. Komsa, G. Ye, X. Chen, T. Hasan, Z. Sun, *ACS Photonics* **2017**, *4*, 3023.
- [21] N. Papadopoulos, R. Frisenda, R. Biele, E. Flores, J. R. Ares, C. Sánchez, H. S. J. van der Zant, I. J. Ferrer, R. D'Agosta, A. Castellanos-Gomez, *Nanoscale* **2018**, *10*, 12424.
- [22] a) S. Niu, G. Joe, H. Zhao, Y. Zhou, T. Orvis, H. Huyan, J. Salman, K. Mahalingam, B. Urwin, J. Wu, Y. Liu, T. E. Tiwald, S. B. Cronin, B. M. Howe, M. Mecklenburg, R. Haiges, D. J. Singh, H. Wang, M. A. Kats, J. Ravichandran, *Nat. Photonics* **2018**, *12*, 392; b) A. Segura, L. Artús, R. Cuscó, T. Taniguchi, G. Cassabois, B. Gil, *Phys. Rev. Mater.* **2018**, *2*, 024001; c) G. A. Ermolaev, D. V. Grudinin, Y. V. Stebunov, K. V. Voronin, V. G. Kravets, J. Duan, A. B. Mazitov, G. I. Tselikov, A. Bylinkin, D. I. Yakubovsky, S. M. Novikov, D. G. Baranov, A. Y. Nikitin, I. A. Kruglov, T. Shegai, P. Alonso-González, A. N. Grigorenko, A. V. Arsenin, K. S. Novoselov, V. S. Volkov, *Nat. Commun.* **2021**, *12*, 854.
- [23] J. Xiong, Q. Yang, Y. Li, S.-T. Wu, *Light Sci Appl* **2022**, *11*, 54.
- [24] Y. Wu, Y. Yang, T. Li, S. Huang, H. Huang, S. Wen, *Appl. Phys. Lett.* **2020**, *117*, 26.
- [25] a) Y. Deng, C. Wu, C. Meng, S. I. Bozhevolnyi, F. Ding, *ACS Nano* **2021**, *15*, 18532; b) S. i. Sande, S. I. Bozhevolnyi, F. Ding, *Nanophotonics* **2023**, *12*, 1363.
- [26] C. Meng, P. C. V. Thrane, F. Ding, S. I. Bozhevolnyi, *Nat. Commun.* **2022**, *13*, 2071.
- [27] N. Yu, F. Capasso, *Nat. Mater.* **2014**, *13*, 139.
- [28] E. O. Fischer, W. Pfab, *Z Naturforsch B* **1952**, *7*, 377.
- [29] a) F. Yu, Q. Lu, S. Zhang, H. Wang, X. Cheng, X. Zhao, *J. Mater. Chem. C* **2015**, *3*, 329; b) D. Yuan, Z. Gao, S. Zhang, Z. Jia, J. Shu, Y. Li, Z. Wang, X. Tao, *Opt. Express* **2014**, *22*, 27606; c) L. Zhang, W. Chen, J. Lu, H. Lin, L. Li, G. Wang, G. Zhang, Z. Lin, *Opt. Mater. Express* **2016**, *6*, 1627.
- [30] a) R. Kronig, *J. Opt. Soc. Am.* **1926**, *12*, 547; b) H. A. Kramers, *Atti Cong. Intern. Fisica* **1927**, *2*, 545.
- [31] M. Shribak, R. Oldenbourg, *Appl. Opt.* **2003**, *42*, 3009.
- [32] L. J. Sham, M. Schlüter, *Phys. Rev. Lett.* **1983**, *51*, 1888.
- [33] S. Nagao, A. Kato, A. Nakajima, K. Kaya, *J. Am. Chem. Soc.* **2000**, *122*, 4221.
- [34] S. Barlow, H. E. Bunting, C. Ringham, J. C. Green, G. U. Bublitz, S. G. Boxer, J. W. Perry, S. R. Marder, *J. Am. Chem. Soc.* **1999**, *121*, 3715.
- [35] a) G. Kresse, J. Furthmüller, *Comput. Mater. Sci.* **1996**, *6*, 15; b) G. Kresse, J. Furthmüller, *Phys. Rev. B* **1996**, *54*, 11169.
- [36] a) P. E. Blöchl, *Phys. Rev. B* **1994**, *50*, 17953; b) G. Kresse, D. Joubert, *Phys. Rev. B* **1999**, *59*, 1758.
- [37] J. P. Perdew, K. Burke, M. Ernzerhof, *Phys. Rev. Lett.* **1996**, *77*, 3865.
- [38] S. Grimme, *J. Comput. Chem.* **2006**, *27*, 1787.
- [39] H. J. Monkhorst, J. D. Pack, *Phys. Rev. B* **1976**, *13*, 5188.
- [40] C. P. Brock, Y. Fu, *Acta Crystallogr. B Struct. Sci.* **1997**, *53*, 928.